A particle-center-averaged Euler-Euler model for monodisperse bubbly flows

Lyu, H.; Lucas, D.; Rzehak, R.; Schlegel, F.;

Originally published:

October 2022

Chemical Engineering Science 260(2022), 117943

DOI: https://doi.org/10.1016/j.ces.2022.117943

Perma-Link to Publication Repository of HZDR:

https://www.hzdr.de/publications/Publ-32958

A particle-center-averaged Euler-Euler model for monodisperse bubbly flows

Hongmei Lyu*, Dirk Lucas, Roland Rzehak, Fabian Schlegel

Institute of Fluid Dynamics, Helmholtz-Zentrum Dresden-Rossendorf, Bautzner Landstrasse 400, 01328 Dresden

Abstract

The standard Euler-Euler model is based on the phase-averaging method. Each bubble force is a function of the local gas volume fraction. As a result, the coherent motion of each bubble as a whole is not enforced when the bubble diameter is larger than the mesh size. However, the bubble force models are typically developed by tracking the bubbles' centers of mass and assuming that the forces act on these locations. In simulations, this inconsistency can lead to a nonphysical gas concentration in the center or near the wall of a pipe when the bubble diameter is larger than the mesh size. Besides, a mesh independent solution may not exist in such cases.

In the present contribution, a particle-center-averaging method is used to average the solution variables for the disperse phase, which allows to represent the bubble forces as forces that act on the bubbles' centers of mass. An approach to simulate bubbly flows is formed by combining the Euler-Euler model framework using the particle-center-averaging method and a diffusion-based method that relates phase-averaged and particle-center-averaged quantities. The remediation of the inconsistency with the standard Euler-Euler model based on phase-averaging method is demonstrated using a simplified two-dimensional test case. The test results illustrate that the particle-center-averaging method can alleviate the over-prediction of the gas volume fraction peak in the channel center and provide mesh independent solutions. Furthermore, a comparison of both approaches is shown for several bubbly pipe flow cases where experimental data are available. The results show that the

*Corresponding author

Email address: h.lyu@hzdr.de (Hongmei Lyu*)

particle-center-averaging method can alleviate the over-prediction of the gas volume fraction peaks in the wall peaking cases as well.

Keywords: particle-center-averaging, phase-averaging, bubble number density, diffusion equation, wall-contact force model, multiphase flow, Euler-Euler model

1. Introduction

Dispersed two-phase flows are widely encountered in chemical engineering, energy production, oil and gas industries and biotechnology. Exploring the flow mechanisms of two-phase flows can ensure safety and improve efficiency of industrial facilities. Many of these flow mechanisms are still not well understood due to their high complexity. Experimental investigations on two-phase flows face the difficulty to measure the flow and distribution of two phases. Hence, they are usually costly and time-consuming. In comparison, simulations provide a more accessible way to study such flows, but they invariably rely on models. Among the simulation methods, the Eulerian two-fluid model shows advantages for simulating bubbly flows up to industrial dimensions with affordable computational cost.

For bubbly flows, air is considered to be the dispersed phase and water is considered to be the continuous phase. In the standard Eulerian two-fluid model, the phase-averaging method is used for both phases. Each bubble force is a function of the gas volume fraction. In this way, the coherent motion of each bubble as a whole is not enforced when the bubble diameter is larger than the mesh size. Hence, the gas belonging to a single bubble can accumulate in a region smaller than the bubble dimension. However, a closure model for a bubble force is typically developed by tracking the trajectories of the bubbles' centers of mass and assuming that a force acts on these locations (Hosokawa et al., 2002; Tomiyama et al., 2002; Ziegenhein et al., 2018). Therefore, an inconsistency exists between the development and the usage of closure models for bubble forces in the standard Euler-Euler model. Consequently, over-prediction of gas volume fraction peaks can appear in the pipe center or near the wall if the bubble diameter is larger than the mesh size (Lehnigk, 2021; Tomiyama et al., 2003).

Applying the particle-center-averaging method (PCAM) has the potential to recover the consistency of the forces in the Euler-Euler model and to form a comprehensive theoretical basis. When using PCAM, bubbles are regarded

as mass points and a bubble number density is introduced into the solution. In this way, the forces act on the bubbles' centers of mass. Zhang and Prosperetti developed a framework for the Euler-Euler model based on PCAM and proposed closure models for the dilute limit by theoretical analysis and direct numerical simulations (Prosperetti, 1998; Zhang and Prosperetti, 1994, 1995, 1997). However, the closure models they developed are for inviscid flow or for rigid interfaces, which cannot be generalized for numerical simulations of bubbly flows. Besides, the calculation of the particle volume fraction from the particle number density in case the particle diameter is larger than the mesh size was not considered. In terms of applications, PCAM was used in the simulation of a wall-bounded bubbly flow by Moraga et al. (2006). However, only a one-way coupling of the phases was considered, i.e., the influence of the disperse phase on the flow of the continuous phase was neglected. To recover the consistency of the Euler-Euler model, Tomiyama et al. (2003) proposed to introduce the bubble number density into the disperse phase continuity equation. However, the turbulent dispersion force in the disperse phase momentum equation is still functions of gas volume fraction, which means that the inconsistencies between the development and the usage of force model still exist. In contrast, Lucas et al. (2001, 2007) introduced a bubble number density in the momentum equation so that bubble forces act on the bubbles' centers of mass and the gas volume fraction is obtained from the convolution of the center-of-mass location and the bubble dimension. However, the solver developed by them is only a one-dimensional solver. A three-dimensional solver is needed to study bubbly flows comprehensively, but it has not been developed so far.

For a PCAM based Euler-Euler model, two different methods are required to average the solution variables for the disperse and the continuous phases, namely particle-center-averaging and phase-averaging method, respectively. Hence, a way to relate the particle-center-averaged and the phase-averaged quantities is needed. The interphase coupling methods used in Euler-Lagrange model can be borrowed to deal with this issue. In bubbly flow simulations with an Euler-Lagrange method, a convolution method with a kernel function is used to transfer Lagrangian quantities to the Eulerian fields and vice versa (Bokkers et al., 2006; Darmana et al., 2006; Lau et al., 2014, 2011). The kernel function represents the influence of the Lagrangian quantities defined at the bubbles' centers of mass on the Eulerian quantities in a certain influence region around the bubbles' centers of mass and vice versa (Lau et al., 2014). However, it is complicated to deal with the kernel

function near curved boundaries or corners of a domain where the boundaries meet non-orthogonally, and to implement it into a code using unstructured meshes and parallel computation (Sun and Xiao, 2015b). A diffusion-based method proposed by Sun and Xiao (2015b) is theoretically equivalent to a convolution method with a Gaussian kernel function and it can give similar results by selecting a suitable diffusion pseudo-time. More importantly, this method is easy to implement for codes using structured or unstructured meshes and serial or parallel processing. Hence, it is used for the coupling of the quantities between the particle-center-averaged and the phase-averaged fields in this study.

In terms of closure models, a baseline model was established at Helmholtz-Zentrum Dresden-Rossendorf (HZDR) for bubbly flows simulations (Rzehak and Krepper, 2015). The baseline model is a set of closure relations for the bubble forces, bubble-induced turbulence and bubble coalescence and breakup. It was validated on a large number of experiments (Fleck and Rzehak, 2019; Hänsch et al., 2021; Krepper et al., 2018; Liao et al., 2016, 2019, 2018, 2020; Rzehak et al., 2017a; Rzehak and Krepper, 2015; Rzehak et al., 2017b; Shi and Rzehak, 2018; Zidouni et al., 2015; Ziegenhein et al., 2013). The validation results show that the baseline model can reproduce the experimental data and provide reasonable simulation results. Therefore, in this study, the baseline model is used as the closure in the bubbly flow simulations. One of the previously used validation databases, namely the MTLoop experiment, will also be used here (Lucas et al., 2005).

In this work, an approach to simulate bubbly flows using PCAM is established by combining the Euler-Euler model based on PCAM, the diffusion-based method relating the the particle-center-averaged and the phase-averaged quantities and the HZDR baseline model for the closure models. In this approach, a physically motivated model for the wall-contact force is introduced to avoid the bubbles' centers of mass coming arbitrarily close to the wall. For this purpose, the wall-contact force model of Lucas et al. (2007) is adapted for oblate ellipsoidal bubbles. The entire approach is implemented based on the solver *reactingTwophaseEulerFoam* in the OpenFOAM Foundation release (OpenFOAM Foundation, 2020). To evaluate its merits and compare it to the standard approach, a simplified two-dimensional test setup is used first. Laminar and turbulent flows are considered separately. A comparison between predictions and experimental measurements is then made for selected tests from the MTLoop experimental database.

2. Theory and solution procedure of particle-center-averaged Euler-Euler model

The theory of the applied Euler-Euler model, the averaging methods as well as the continuity and momentum equations from Prosperetti (1998) are summarized in this section. The way to relate the phase-averaged and the particle-center-averaged quantities will be introduced. Besides, the diffusion pseudo-time optimization and the proposed correction terms will be explained. Finally, the solution procedure will be briefly mentioned. In this study, both phases are taken as incompressible and a fixed bubble size (monodisperse) is assumed.

2.1. Phase-averaging and particle-center-averaging method

The phase-averaging is used to average the solution variables for the continuous phase. The phase-averaging of a quantity f of phase k is defined by

$$\overline{f_k} = \frac{1}{\alpha_k} \int_{C^N} f_k X_k P\left(N,t\right) dC^N, \tag{1}$$

where X_k is the phase indicator function. It is 1 where the phase k exists, otherwise it is 0. In Eq. (1), C^N describes the set of all possible dynamic states of the system containing N bubbles and $P\left(N,t\right)$ is the probability density function of a dynamic state at time t. Note, the indistinguishable particle probability is used here, so

$$\int_{C^N} P\left(N,t\right) dC^N = 1. \tag{2}$$

Hence, $N!$ does not appear in the definition of the averaged quantities. The volume fraction of phase k is defined by

$$\alpha_k = \int_{C^N} X_k P\left(N,t\right) dC^N. \tag{3}$$

In this study, "particle" and "bubble" are used interchangeably since the formalism is the same, but only applications for bubbly flows are considered. PCAM is used to average the solution variables for the disperse phase. It is suitable to average quantities that concern the particle as a whole, like the center-of-mass velocity. Therefore, the delta function δ indicating the location of the particle center is involved in the average (Biesheuvel and Gorissen,

1990; Moraga et al., 2006; Prosperetti, 1998; Zhang and Prosperetti, 1994). The particle-center-averaging of a quantity f is defined by

$$\langle f \rangle (\boldsymbol{x}, t) = \frac{1}{n} \int_{C^N} \left[\sum_{i=1}^{N} \delta \left(\boldsymbol{x} - \boldsymbol{y}^i \right) f^i (N, t) \right] P (N, t) \, dC^N, \tag{4}$$

where $\boldsymbol{x}$ is the spatial location, f^i is the value of the quantity f for bubble i ($i = 1, \ \cdots, \ N$), and $\boldsymbol{y}^i$ is the location of its center. The bubble number density is defined by

$$n = \int P (\boldsymbol{x}, \boldsymbol{u}, t) \, d\boldsymbol{u}. \tag{5}$$

Here $P (\boldsymbol{x}, \boldsymbol{u}, t)$ is the one-bubble probability density function, which is related to $P (N, t)$ as

$$P (\boldsymbol{x}, \boldsymbol{u}, t) = \int P (N, t) \, dC^{N-1}. \tag{6}$$

The product of n and $d\boldsymbol{x}$ represents the probability of finding a bubble center in the vicinity of the location $\boldsymbol{x}$ at time t.

$$\int n d\boldsymbol{x} = N. \tag{7}$$

This relation justifies that n is the bubble number density.

2.2. Continuity and momentum equations

The continuity equation for the continuous phase is the same as in the standard Euler-Euler model (Drew and Passman, 1998)

$$\frac{\partial \alpha_c \rho_c}{\partial t} + \boldsymbol{\nabla} \cdot (\alpha_c \rho_c \overline{\boldsymbol{u}_c}) = 0, \tag{8}$$

where ρ is the density and $\boldsymbol{u}$ is the velocity. Here and in the following, a subscript c denotes a quantity for the continuous phase while a subscript d denotes a quantity for the disperse phase. For the disperse phase, the continuity equation becomes a transport equation for the bubble number density

$$\frac{\partial n \rho_d}{\partial t} + \boldsymbol{\nabla} \cdot (n \rho_d \langle \boldsymbol{u}_d \rangle) = 0. \tag{9}$$

The momentum equation for the continuous phase is

$$\begin{aligned}&\frac{\partial \alpha_c \rho_c \overline{\boldsymbol{u}_c}}{\partial t} + \boldsymbol{\nabla} \cdot \left(\alpha_c \rho_c \, \overline{\boldsymbol{u}_c} \, \overline{\boldsymbol{u}_c}\right) \\ &= -\alpha_c \nabla \overline{p_c} + \alpha_c \boldsymbol{\nabla} \cdot \overline{\mathbf{S}_c} + \boldsymbol{\nabla} \cdot \left(\alpha_c \overline{\mathbf{T}_c}\right) + \overline{\boldsymbol{f}_c} + \alpha_c \rho_c \boldsymbol{g},\end{aligned} \tag{10}$$

where p, $\mathbf{S}$, $\mathbf{T}$, $\boldsymbol{f}$ and $\boldsymbol{g}$ are pressure, viscous stress tensor, Reynolds stress tensor, interfacial force per unit volume and acceleration of gravity, respectively. The momentum equation for the disperse phase is derived by averaging the equation of motion for bubbles (Prosperetti, 1998; Zhang and Prosperetti, 1994). The momentum equation is

$$\begin{aligned}&\frac{\partial \beta_d \rho_d \left\langle \boldsymbol{u}_d \right\rangle}{\partial t} + \boldsymbol{\nabla} \cdot \left(\beta_d \rho_d \left\langle \boldsymbol{u}_d \right\rangle \left\langle \boldsymbol{u}_d \right\rangle\right) \\ &= -\beta_d \nabla \overline{p_c} + \beta_d \boldsymbol{\nabla} \cdot \left\langle \mathbf{S}_c \right\rangle + \boldsymbol{\nabla} \cdot \left(\beta_d \left\langle \mathbf{T}_d \right\rangle\right) + \left\langle \boldsymbol{f}_d \right\rangle + \beta_d \rho_d \boldsymbol{g},\end{aligned} \tag{11}$$

where β_d is gas volume fraction projecting all the bubble volume to the bubble centers. It is calculated by

$$\beta_d = n V_d, \tag{12}$$

where V_d is the bubble volume.

It should be mentioned that some assumptions and simplifications have been used to derive Eqs. (10) and (11) from the original momentum equations in Prosperetti (1998). First, the collision stress due to direct bubble-bubble interactions is not considered in Eq. (11). Second, the terms containing $A[\boldsymbol{\sigma}_c]$ in the momentum equations in Prosperetti (1998) are regarded as the interfacial momentum interactions and replaced by $\overline{\boldsymbol{f}_c}$ and $\langle \boldsymbol{f}_d \rangle$. At last, the surface stress term $L[\boldsymbol{\sigma}_c]$ in the momentum equation of the continuous phase in Prosperetti (1998) originates from the non-uniform distribution of pressure force on the surface of a bubble or a particle (Zhang and Prosperetti, 1994). It is neglected since no closure model for it is known in a bubbly flow.

Compared to the momentum equations and the way to derive the equations in the standard Euler-Euler model (Drew and Passman, 1998), the differences lie in:

1. The phase volume fraction in the viscous stress term of Eq. (10) is outside of the divergence since the part of the viscous stress term related to the gradient of the phase volume fraction is cancelled by the interfacial contributions, which is similar to the pressure term (Prosperetti and Jones, 1984).

2. Equation (11) is derived by averaging the equation of motion for bubbles, while the equation in the standard Euler-Euler model is derived by averaging the local instantaneous momentum equation and by using the phase indicator function of the disperse phase.
3. The physical meaning of the momentum equation for the disperse phase in the Euler-Euler model based on PCAM is different from that in the standard Euler-Euler model. Equation (11) displays the momentum balance of gas, which belongs to bubbles having their centers located inside the control volume. This gas may only be partially contained within the control volume. In the standard Euler-Euler model, the equation refers to the momentum balance of all gas contained inside the control volume. This gas may belong partially or even completely to bubbles with centers outside of the control volume. Hence, Eq. (11) is related to the bubble number density, while in the standard Euler-Euler model, the momentum equation of the disperse phase is related to the volume fraction of the disperse phase.
4. Equation (11) explicitly shows the response of bubbles to the pressure and the viscous stress tensor of the continuous phase. Hence, no additional closure model for the viscous stress tensor of the disperse phase is required. In the standard Euler-Euler model, the viscous stress tensor of the disperse phase appears and a closure model for it is needed.

2.3. Closure models

The selected closure models for the interfacial forces according to the HZDR baseline model, which is based on the standard Euler-Euler model, are listed in Table 1. In the standard Euler-Euler model, the interfacial

Table 1: HZDR baseline model for monodisperse bubbly flows.

Force and turbulence	Selected model
Drag force	Ishii and Zuber (1979)
(Shear-) lift force	Tomiyama et al. (2002) with cosine wall damping
Turbulent dispersion force	Burns et al. (2004)
Wall (-lift) force	Hosokawa et al. (2002)
Virtual mass force	Constant coefficient, $C_{\mathrm{VM}} = 0.5$
Turbulence	$k-\omega$ SST
Bubble-induced turbulence	Ma et al. (2017)

forces are functions of the gas volume fraction. In the Euler-Euler model based on PCAM, the interfacial forces for the disperse phase are changed to be functions of the bubble number density. The necessary conversion is achieved by

$$\boldsymbol{f}\left(n\right)=\frac{nV_d}{\alpha_d}\boldsymbol{f}\left(\alpha_d\right), \tag{13}$$

where $\boldsymbol{f}\left(n\right)$ and $\boldsymbol{f}\left(\alpha_d\right)$ are the force per unit volume as a function of the bubble number density and the gas volume fraction, respectively. For the turbulent dispersion force model, an additional change is needed for the term $\nabla\alpha_d/\alpha_d$, which should be changed to $\nabla\beta_d/\beta_d$ based on the derivation procedure in Burns et al. (2004, see appendix).

Moreover, for the PCAM based Euler-Euler model, an additional wall-contact force has to be introduced to prevent the bubbles' centers of mass from coming nonphysically close to the wall. For this purpose, the wall-contact force model proposed by Lucas et al. (2007) is adopted for bubbles with an oblate ellipsoidal shape. The resulting wall-contact force $\boldsymbol{f}_d^{contact}$ reads

$$\boldsymbol{f}_d^{contact}=-\pi d_B\sigma n\left\{-\frac{1}{\widetilde{L}^2}+\frac{3\widetilde{L}}{2G}\left[\left(\frac{4\sqrt{G}}{3}+\frac{\widetilde{L}^3}{\sqrt{G}}\right)\operatorname{arctanh}\sqrt{G}-1\right]\right\}, \tag{14}$$

where $\widetilde{L}=2L/d_B$ and $G=1-\widetilde{L}^3$. In these equations, d_B is the bubble diameter, σ is the surface tension coefficient and L is the distance between the bubble's center-of-mass and the wall.

For turbulent flows, the continuous phase turbulence is simulated by the turbulence models in Table 1, while the flow of the disperse phase is assumed to be laminar since $\rho_d \ll \rho_c$.

2.4. Coupling between phase-averaged and particle-center-averaged quantities

As discussed above, phase-averaging and particle-center-averaging are used to average the solution variables for the continuous phase and the disperse phase, respectively. When the bubble diameter is smaller than the mesh size, the difference between phase-averaged and particle-center-averaged quantities is not significant. In this condition, it is reasonable to assume that a phase-averaged quantity approximately equals the corresponding particle-center-averaged quantity (i.e. $\alpha_d \approx \beta_d$). However, when the bubble diameter is larger than the mesh size, the difference between the

averaging methods becomes significant, and this assumption is not appropriate. Therefore, a comprehensive way is needed to couple phase-averaged and particle-center-averaged quantities, which can be used in both conditions. In principle this way could be established by a convolution using a kernel function that represents the spatial extent of a single bubble (Lyu et al., 2020). However, implementing such a method efficiently in a numerical simulation using unstructured grids is difficult. Therefore, a diffusion-based method is used here to relate phase-averaged and particle-center-averaged quantities. The bubble influence region, over which the diffusion takes place, may be larger than the actual bubble volume to comprise also effects of bubble shape and path oscillations.

To calculate a phase-averaged quantity from the corresponding particle-center-averaged quantity, the quantity in the bubble's center-of-mass should be distributed. For example, to calculate the gas volume fraction from the bubble number density, the bubble volume is distributed around its center-of-mass by solving the following diffusion equation

$$\frac{\partial \alpha_d}{\partial \tau} - \boldsymbol{\nabla} \cdot (C_{\text{diff}} \nabla \alpha_d) = 0, \tag{15}$$

with an initial condition of $\alpha_d = nV_d$. In this process, the gas volume is conserved. In the equation, τ is the diffusion pseudo-time and C_{diff} is the diffusion coefficient, both determining the size of the bubble influence region. Note, this diffusion process takes place at every time step of the simulation such that τ is unrelated to the physical time, and, hence, referred to as a pseudo-time. Without loss of generality, C_{diff} is set to be 1 $\mathrm{m^2\,s^{-1}}$ for all diffusion processes in the present study, while an optimized value is determined for τ in section 2.5. To solve Eq. (15), a Neumann boundary condition with derivative equal to zero is used for all boundaries.

Similarly, to calculate a phase-averaged gas velocity $\overline{\boldsymbol{u}_d}$, the bubble momentum is distributed about its center-of-mass by the following diffusion equation

$$\frac{\partial \alpha_d \overline{\boldsymbol{u}_d}}{\partial \tau} - \boldsymbol{\nabla} \cdot (C_{\text{diff}} \nabla (\alpha_d \overline{\boldsymbol{u}_d})) = 0, \tag{16}$$

with an initial condition of $\alpha_d \overline{\boldsymbol{u}_d} = n \langle \boldsymbol{u}_d \rangle V_d$. Other settings are as described above.

Besides, the forces acting on the bubble centers are distributed to the

bubble influence region by the following diffusion equation

$$\frac{\partial \overline{\boldsymbol{f}_d}}{\partial \tau} - \boldsymbol{\nabla} \cdot \left(C_{\text{diff}} \nabla \overline{\boldsymbol{f}_d} \right) = 0, \tag{17}$$

with an initial condition of $\overline{\boldsymbol{f}_d} = \langle \boldsymbol{f}_d \rangle$. The total force does not change in this process. Finally, the forces acting on the continuous phase can be calculated by

$$\overline{\boldsymbol{f}_c} = -\overline{\boldsymbol{f}_d}. \tag{18}$$

On the contrary, the continuous phase velocity at the bubbles' centers of mass $\langle \boldsymbol{u}_c \rangle$ can be calculated from the corresponding phase-averaged continuous phase velocity $\overline{\boldsymbol{u}_c}$ by the following weighted average

$$\langle \boldsymbol{u}_c \rangle (\boldsymbol{x}, \tau) = \int_{-\infty}^{+\infty} \overline{\boldsymbol{u}_c} (\boldsymbol{x_0}, 0) \frac{1}{(4\pi C_{\text{diff}} \tau)^{\frac{3}{2}}} \exp\left\{ -\frac{(\boldsymbol{x} - \boldsymbol{x_0})^2}{4 C_{\text{diff}} \tau} \right\} d\boldsymbol{x_0}, \tag{19}$$

which is the solution of

$$\frac{\partial \langle \boldsymbol{u}_c \rangle}{\partial \tau} - \boldsymbol{\nabla} \cdot (C_{\text{diff}} \nabla \langle \boldsymbol{u}_c \rangle) = 0, \tag{20}$$

with an initial condition of $\langle \boldsymbol{u}_c \rangle (\boldsymbol{x}_0, 0) = \overline{\boldsymbol{u}_c} (\boldsymbol{x}_0, 0)$, where $\boldsymbol{x_0}$ is the spatial coordinate vector.

2.5. Diffusion pseudo-time optimization

A key parameter in the conversions using the diffusion-based method is the diffusion pseudo-time τ. The diffusion pseudo-time is independent of the physical time. It affects the size of the bubble influence region.

The size of the bubble influence region in the convolution or the diffusion-based method is still an open question. Deen et al. (2004) and Darmana et al. (2006) set this size to be 3 times the bubble mean diameter. However, Bokkers et al. (2006) and Lau et al. (2011) set it to be 6 and 2 times the bubble mean diameter, respectively. Besides, Sun and Xiao (2015a) argued that this size should approximately equal the size of the wake of the particles. Since no agreement on the value for the bubble influence region is found in literature, this subsection aims to optimize the diffusion pseudo-time by minimizing the difference between expected and numerically computed gas volume fractions in a simplified one-dimensional case.

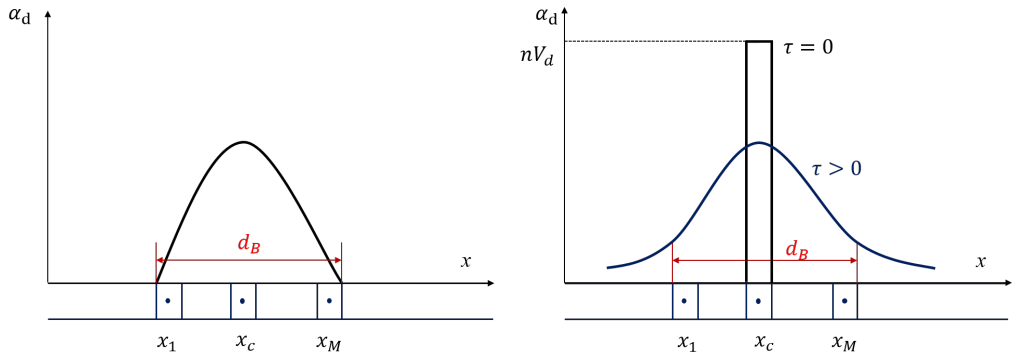

(a) Expected gas volume fraction.

(b) Solved gas volume fraction.

Figure 1: Gas volume fraction for the one-dimensional case

In the condition that a layer of equally sized and spherical bubbles slides on a wall, Lubchenko et al. (2018) derived a fixed profile for the gas volume fraction near the wall in the direction perpendicular to the wall. This profile can be used as the expected gas volume fraction in a one-dimensional case where a stream of spherical bubbles is injected at location $x = x_c$. Hence, the expected gas volume fraction reads

$$\alpha_d^{\exp}(x) = \begin{cases} \alpha_{\max} - 4\alpha_{\max}(x - x_c)^2 / d_B^2, & |x - x_c| \le d_B \\ 0, & |x - x_c| > d_B \end{cases}, \tag{21}$$

where x is the spatial coordinate and $\alpha_{\max}$ is the maximum gas volume fraction.

The gas volume fraction is obtained by solving Eq. (15) in one dimension (Haberman, 2012)

$$\alpha_d(x, \tau) = \int_{-\infty}^{+\infty} n(x_0, 0) V_d \frac{1}{\sqrt{4\pi C_{\text{diff}} \tau}} \exp\left\{ -\frac{(x - x_0)^2}{4 C_{\text{diff}} \tau} \right\} dx_0. \tag{22}$$

In the one-dimensional case concerned here, the initial bubble number density is concentrated only in one mesh cell. Consequently, the solved gas volume fraction can be discretized as

$$\alpha_d^{\text{sol}}(x, \tau) \approx n(x_c, 0) V_d \frac{1}{\sqrt{4\pi C_{\text{diff}} \tau}} \exp\left\{ -\frac{(x - x_c)^2}{4 C_{\text{diff}} \tau} \right\} \Delta_x, \tag{23}$$

where Δ_x is the size of the grid cell containing the bubble centers.

In the comparison of the expected and the solved gas volume fractions, the gas volume is kept the same by setting

$$n\left(x_c, 0\right) = \frac{\sum_{i=1}^{M} \alpha_d^{\exp}\left(x_i\right) V_i}{V_d V_c}, \tag{24}$$

where M is the number of cells covered by the bubbles (Fig. 1(a)), while V_i and V_c are the volumes of the grid cell i and c, respectively.

The optimized diffusion pseudo-time is the time for the error to reach its minimum value

$$E\left(\tau\right) = \sum_{i=1}^{M} \left[\alpha_d^{\exp}\left(x_i, \tau\right) - \alpha_d^{\mathrm{sol}}\left(x_i, \tau\right)\right]^2, \tag{25}$$

where $x_i \in \left(x_c \pm 0.5\ d_B\right)$.

In the last equation, the discretised form of α_d^{sol} is used. The influence of the parameter M, which is used in the discretisation on the optimized diffusion pseudo-time, should be analyzed. Since the optimized diffusion pseudo-time τ_{opt} will depend on C_{diff} as well as d_B, a dimensionless optimized diffusion pseudo-time

$$\widetilde{\tau}_{\mathrm{opt}} = \frac{\tau_{\mathrm{opt}} C_{\mathrm{diff}}}{d_B^2} \tag{26}$$

will be used in the analysis. The result is shown in Fig. 2.

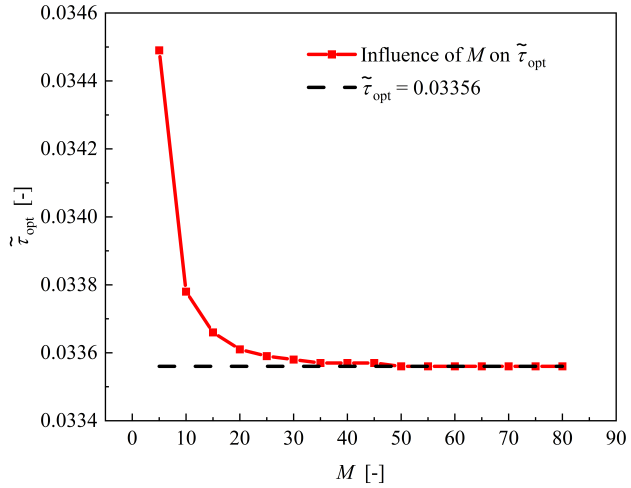

Figure 2: Mesh sensitivity analysis for the dimensionless optimized diffusion pseudo-time.

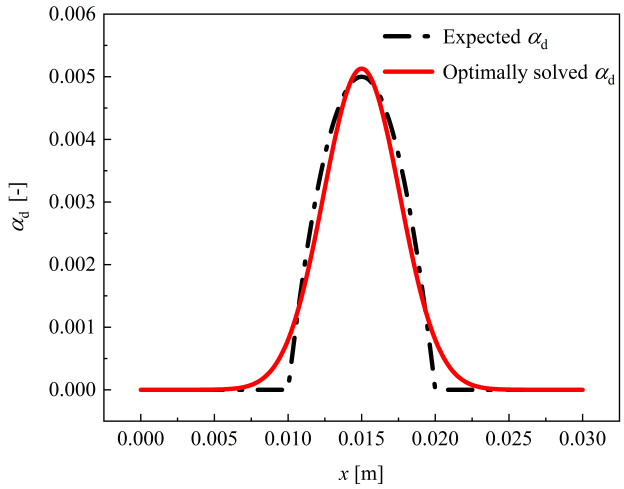

Figure 3: Expected and optimally solved gas volume fraction for the one-dimensional case.

As can be seen, $\widetilde{\tau}_{\text{opt}}$ is almost a constant when M is larger than 30. As a result, $\widetilde{\tau}_{\text{opt}} = 0.03356$ is used in the following simulations. With the optimized diffusion pseudo-time, the distributions of the expected and the solved gas volume fractions for the one-dimensional case can be seen in Fig. 3. For the solved gas volume fraction, 94.72% of the gas volume is contained within $x_c \pm 0.5\ d_B$.

2.6. Correction terms for drag and virtual mass force of continuous phase

In the OpenFOAM multiphase flow solvers for the Euler-Euler model, the drag and virtual mass force are treated semi-implicitly to make the solution stable. After changing the forces to act on the bubble centers based on Eq. (13) and using the particle-center-averaged fields, the drag force and the virtual mass force for the disperse phase are

$$\left\langle \boldsymbol{f}_d^{\text{drag}} \right\rangle = -\frac{3}{4d_B} C_D \rho_c \beta_d |\langle \boldsymbol{u}_d \rangle - \langle \boldsymbol{u}_c \rangle| \left([\langle \boldsymbol{u}_d \rangle] - \langle \boldsymbol{u}_c \rangle \right) \tag{27}$$

and

$$\left\langle \boldsymbol{f}_d^{\text{VM}} \right\rangle = -C_{\text{VM}} \rho_c \beta_d \left(\frac{D_d \left[\langle \boldsymbol{u}_d \rangle \right]}{Dt} - \frac{D_c \langle \boldsymbol{u}_c \rangle}{Dt} \right), \tag{28}$$

respectively, where C_D and C_{VM} are the coefficients and ρ is the density. The quantities within the square brackets are the quantities remaining to be solved. They are treated implicitly. Note, the other term in Eq. (27) involving $\langle \boldsymbol{u}_d \rangle$ is treated explicitly, which means the old value from the last time or

iteration step will be used. The forces $\left\langle \boldsymbol{f}_d^{\mathrm{drag}} \right\rangle$ and $\left\langle \boldsymbol{f}_d^{\mathrm{VM}} \right\rangle$ can be calculated directly using the particle-center-averaged fields, and hence, appear directly on the right hand side of the disperse phase momentum equation.

To keep the forces consistent, these forces, which act on the bubbles' centers of mass are converted to phase-averaged forces acting on the continuous phase using Eqs. (17) and (18). However, this conversion requires an explicit implementation, which will cause numerical stability problems. As a solution, besides the conversion, a correction term

$$\boldsymbol{f}_c^{\mathrm{drag,\,correction}} = -\frac{3}{4d_B} C_D \rho_c \beta_d |\langle \boldsymbol{u}_d \rangle - \langle \boldsymbol{u}_c \rangle| \left([\overline{\boldsymbol{u}_c}] - \overline{\boldsymbol{u}_c} \right) \tag{29}$$

is added to the drag force of the continuous phase, while a correction term

$$\boldsymbol{f}_c^{\mathrm{VM,\,correction}} = -C_{\mathrm{VM}} \rho_c \beta_d \left(\left[\frac{D_c \overline{\boldsymbol{u}_c}}{Dt} \right] - \frac{D_c \overline{\boldsymbol{u}_c}}{Dt} \right) \tag{30}$$

is added to the virtual mass force of the continuous phase.

These correction terms do not exist in theory. However, once the simulation has sufficiently converged to a steady state, these terms will be neglectable since the difference between the current and the old values will be neglectable.

2.7. Solution procedure

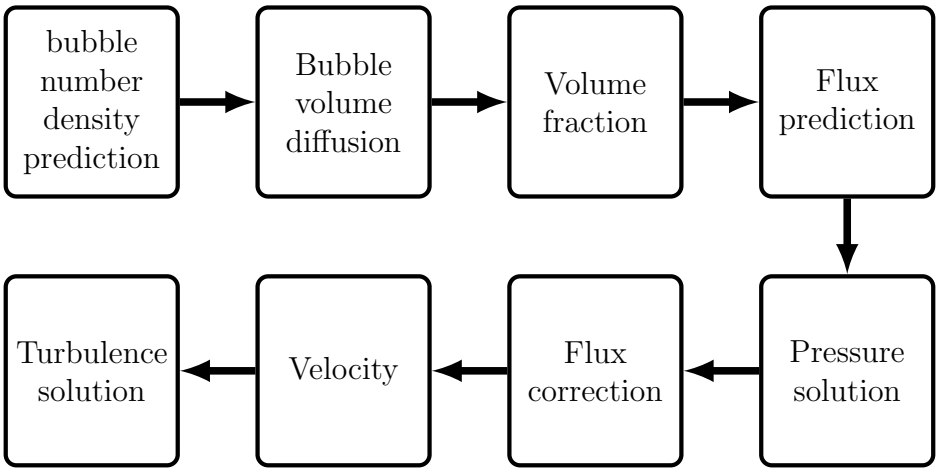

Figure 4: Solution procedure.

For the numerical solution, the underlying equations are discretised by the finite volume method. For the conservation equations in section 2.2, a first order Euler implicit scheme is used for the temporal discretisation and a flux-limiter is used for the discretisation of the convection term. For the pressure and velocity coupling, the PISO (Pressure Implicit with Splitting of Operator) algorithm is used. Besides, it is assumed that particle-center-averaged and phase-averaged pressure is the same. Moreover, for the diffusion equations in section 2.4, which are used to couple the phase-averaged and particle-center-averaged quantities, an Euler implicit scheme is used in the temporal discretisation and a Gauss linear scheme is used for the discretisation of the laplacian term. The solution procedure is shown in Fig. 4.

3. Basic verification of the improvement of Euler-Euler model based on the particle-center-averaging method

In this section, a simplified two-dimensional test case is used to reveal the numerical problems and nonphysical results of the standard Euler-Euler model caused by the inconsistency in the bubble force models. Besides, the improvement by changing the bubble forces to act on the bubbles' centers of mass by PCAM is shown.

3.1. Geometry and simulation setups

A two-dimensional test case similar to that used in Tomiyama et al. (2003) is employed. The domain and boundary settings are shown in Fig. 5 (a). It is a rectangle with a size of 0.03 m $\times$ 0.5 m. A stream of air bubbles is injected at $x = 0$ and $y = 0$ into the domain that contains only water at the beginning. The inlet liquid velocity is a parabolic profile (Fig. 5 (b)) to introduce a shear flow field, while the inlet gas velocity is uniform with a value of 0.1 $\mathrm{m\,s^{-1}}$. Besides, the inlet gas volume fraction distribution for the simulations with the standard Euler-Euler model is shown in Fig. 5 (c). In this profile, the lateral length over which the gas volume fraction is non-zero equals the bubble diameter.

For the PCAM Euler-Euler simulations, bubble number density at the inlet is non-zero only in the center cell of the mesh. To keep the inlet gas flow rate the same as in the standard Euler-Euler simulation, the inlet bubble number density is calculated by

$$n = \frac{1}{V_d} \sum_{j=1}^{M} \alpha_{d,j}, \tag{31}$$

where $\alpha_{d,j}$ is the gas volume fraction in mesh cell j, M is the number of mesh cells in the first layer near the inlet containing non-zero gas volume fraction, and the mesh aspect ratio is kept at a value of 1 (i.e. grid spacing $\Delta = \Delta_x = \Delta_y$).

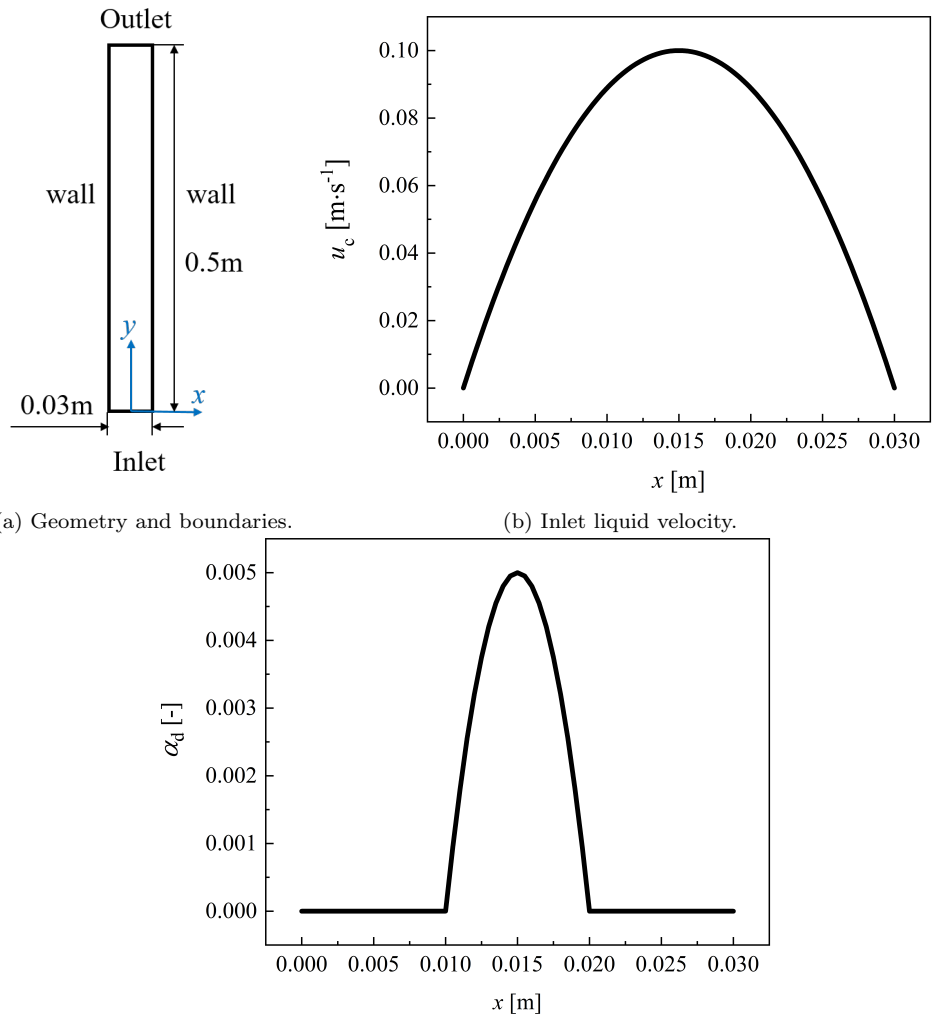

(a) Geometry and boundaries.

(b) Inlet liquid velocity.

(c) Inlet gas volume fraction

Figure 5: Geometry and boundary conditions

Table 2: Boundary settings.

Variable	Inlet	Wall	Outlet
α_d/α_c	fixedValue	zeroGradient	zeroGradient
n/β_d	fixedValue	fixedValue (0)	zeroGradient
U_d	fixedValue	slip	pressureInletOutletVelocity
U_c	fixedValue	noSlip	pressureInletOutletVelocity
p_{rgh}	fixedFluxPressure	fixedFluxPressure	prghPressure
p	calculated	calculated	calculated

Table 3: Physical properties of the fluids (μ: dynamic viscosity).

ρ_c [kg m^{-3}]	ρ_d [kg m^{-3}]	μ_c [kg m^{-1} s^{-1}]	μ_d [kg m^{-1} s^{-1}]
995.6	1.165	7.97e-4	1.86e-05

The detailed boundary settings are listed in Table 2. Note, OpenFOAM solver works with a pseudo pressure p_{rgh} instead of p to treat the machine precision issues. Their relation is

$$p = p_{\mathrm{rgh}} + \rho_m g h, \tag{32}$$

where ρ_m is the mixture density. It is calculated by

$$\rho_m = \alpha_d \rho_d + \alpha_c \rho_c. \tag{33}$$

In all simulations, the Courant number is 0.002. Besides, the temperature of air and water is 25 °C and the pressure is 101325 Pa. The physical properties of the fluids are shown in Table 3.

3.2. Mesh sensitivity analysis

A mesh sensitivity is carried out for the standard Euler-Euler model and the PCAM Euler-Euler simulation. In this analysis, the ratio between the bubble diameter and the size of the mesh cells ranges from 2.5 to 20. Since the simulations of the standard Euler-Euler model do not reach a steady state, the results for the gas volume fraction α_d are averaged between 5 s and 20 s of simulation time at an axial height of $y = 0.4$ m. Laminar and turbulent flow cases are considered separately.

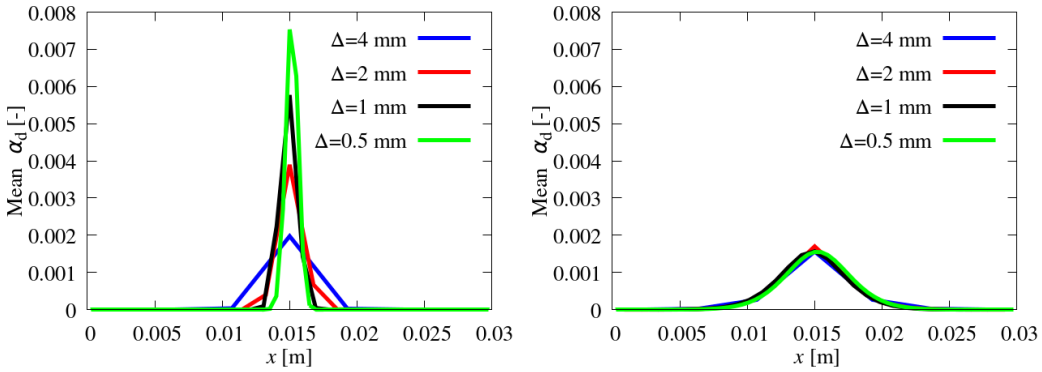

(a) Standard Euler-Euler model.

(b) Euler-Euler model based on PCAM.

Figure 6: Mesh sensitivity analysis for the laminar flow case (Δ: grid spacing)

For a laminar flow, the results of the mesh sensitivity analysis are shown in Fig. 6. For the standard Euler-Euler model, the peak of the gas volume fraction increases continuously with decreasing mesh size. This results from the fact that the lift force acts on the distributed gas and drives it to the mesh cells in the channel center. The resulting concentration of gas in the channel center becomes higher when the mesh is refined and mesh independent results cannot be found. In contrast, in the results of the Euler-Euler simulation based on PCAM, the gas volume fraction distributions are similar upon refining the mesh. The reason is that in this method, the bubble forces are changed to act on the bubbles' centers of mass and these centers are located at the centreline of the channel, where the shear gradient vanishes. Therefore, the PCAM remedies the numerical deficiency in the standard Euler-Euler approach and provides a mesh independent solution for laminar flow.

For a turbulent flow, the results of the mesh sensitivity analysis are shown in Fig. 7 and show overall similar results as for the laminar flow. In the results of the standard Euler-Euler model, the gas volume fraction peak for a mesh size of 0.5 mm is slightly lower than the peak in the laminar flow. The reason is that the turbulent dispersion force flattens the gas volume fraction peak. For other mesh sizes, the gas volume fraction peaks in the laminar and the turbulent flow case are almost the same. As a result, the phenomenon that the gas volume fraction peak grows with decreasing mesh size is still significant. After using PCAM, the gas volume fractions remain

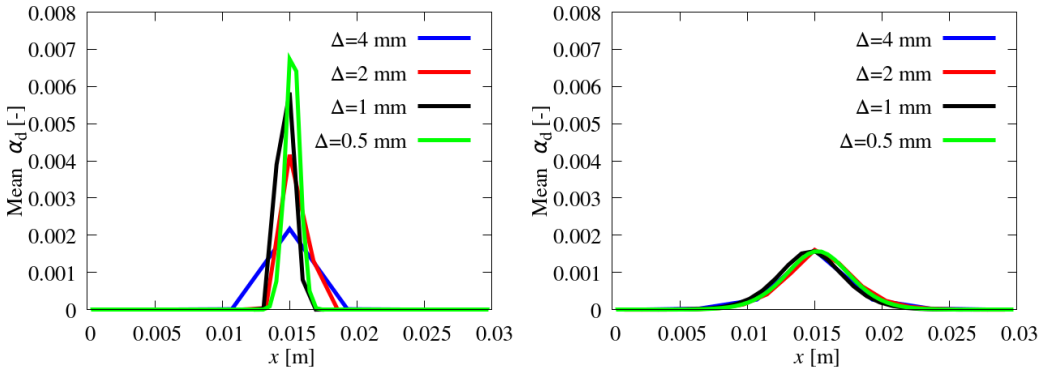

(a) Standard Euler-Euler model.

(b) Euler-Euler model based on PCAM.

Figure 7: Mesh sensitivity analysis for the turbulent flow case (Δ: grid spacing)

similar upon refining the mesh.

In summary, using PCAM in the Euler-Euler model yields a mesh independent solution, where the standard Euler-Euler model does not. However, these test cases are simplified. It is conceivable that mesh independent solutions may exist also for the standard Euler-Euler model when the turbulent dispersion force is strong enough.

3.3. Axial development of gas volume fraction

In this subsection, the axial development of the gas volume fractions is analyzed. The grid spacing for all simulations in this subsection is 2 mm. At the inlet, the lateral region between $x = 0.01$ and $x = 0.02$ has non-zero gas volume fractions, which is equal to the bubble diameter.

For a laminar flow, the simulation results are shown in Fig. 8. In the results for the standard Euler-Euler model, the gas volume fraction profiles are narrow with high peak, which means that gas concentrates in the channel center following the flow downstream. Besides, the lateral region covered by the gas becomes smaller than the bubble diameter, which is nonphysical. This phenomenon is caused again by the lift force, which transports the distributed gas to the channel center even though it really belongs to the same bubble. In contrast, by using PCAM in the Euler-Euler model, the distribution of the gas volume fraction remains almost unchanged after the inlet (Fig. 8 (b)). Besides, the width of the region covered by the gas has a size close to the bubble diameter. Therefore, the gas volume fractions predicted by PCAM are considered to be more reasonable.

In turbulent flow, the simulation results are shown in Fig. 9. In the results of the standard Euler-Euler model, the gas over-concentration in the channel center downstream of the inlet is still significant although it does not change anymore. After changing the forces to act on the bubbles' centers of mass by PCAM, the over-concentration of the gas in the channel center disappears from the simulation results.

In conclusion, gas over-concentration can appear in the channel center in the standard Euler-Euler model since lift force is a function of the gas volume fraction. This gas over-concentration is avoided by changing the bubble forces to act on the bubbles' centers of mass as done by PCAM.

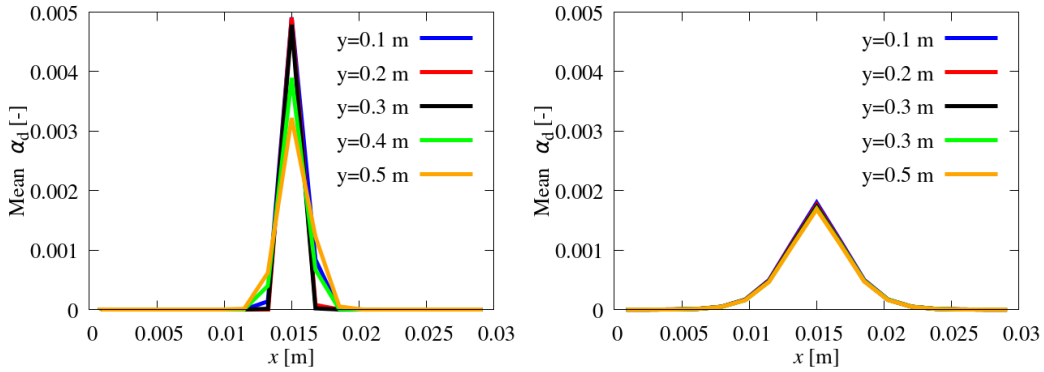

(a) Standard Euler-Euler model. (b) Euler-Euler model based on PCAM.

Figure 8: Gas volume fraction for laminar flow at different downstream positions

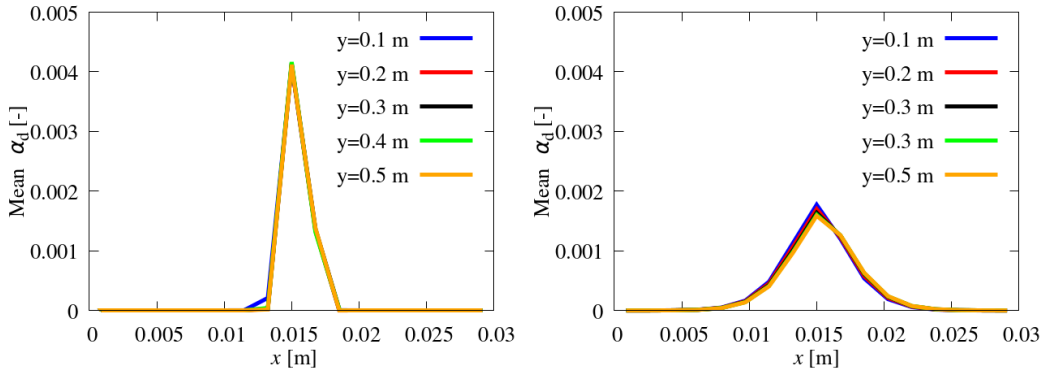

(a) Standard Euler-Euler model. (b) Euler-Euler model based on PCAM.

Figure 9: Gas volume fraction for turbulent flow at different downstream positions

4. Comparisons of simulation results and experimental data in bubbly pipe flows

4.1. Experimental conditions

To evaluate PCAM in the Euler-Euler model, the results of the standard Euler-Euler model and the Euler-Euler simulations based on PCAM are compared with the measurement data from the MTLoop experiment (Lucas et al., 2005). The test section in the experiment is a vertical pipe. Its inner diameter is 51.2 mm. The temperature of air and water in the experiment is 30 °C and the pressure is 101325 Pa. The data used for comparison are measured at a distance of 3.03 m from the gas injection. At this level, the ratio between the distance from the gas inlet and the pipe diameter is about 59. Therefore, a fully-developed flow is expected.

4.2. Simulation setup

To reduce the computational cost, the geometry in the simulations is a wedge with a center angle of 1.0 degree. The axial length of the wedge is 3.5 m. A wedge boundary condition is used in the circumference direction. The numbers of mesh cells in the radial and the axial directions are 50 and 800, respectively. The mesh spacing is uniform in both directions. At the inlet, a uniform profile for the velocity and the phase fraction of each phase is used. The values are calculated from the superficial air and water velocities by assuming that the relative velocity between the disperse and continuous phases is zero at the inlet. The detailed boundary settings are listed in Table 2. Besides, the parameters for the selected cases are listed in Table 4. The selected cases comprise different flow regimes, namely flows with wall peaking and center peaking gas volume fraction profiles as well as finely dispersed bubbly flows.

4.3. Comparison of wall peaking cases

If the gas volume fraction peaks are located near the wall and the bubble diameters are larger than the mesh size, the gas volume fraction peaks simulated by the standard Euler-Euler model can be over-predicted. In Fig. 10, the gas volume fraction peaks of the cases 43, 20, 98, 42 and 109 simulated by the standard Euler-Euler model are about 590%, 170%, 170%, 70% and 70% higher than the peaks in the experimental data, respectively. The extent of over-prediction is influenced by the magnitude of the radial resultant force

Table 4: Parameters for the selected MTLoop cases (J: superficial velocity; Δ: radial grid spacing).

Name	J_c [$\mathrm{m\,s^{-1}}$]	J_d [$\mathrm{m\,s^{-1}}$]	α_d %	d_B [mm]	d_B/Δ
19	1.0170	0.0040	0.43	4.697	9.2
20	1.6110	0.0040	0.30	3.610	7.1
30	1.0170	0.0062	0.63	4.962	9.7
35	0.0641	0.0096	3.78	6.619	12.9
41	1.0170	0.0096	0.95	5.114	10.0
42	1.6110	0.0096	0.68	4.151	8.1
43	2.5540	0.0096	0.47	2.918	5.7
47	0.1020	0.0151	5.08	7.442	14.5
48	0.1610	0.0151	4.23	6.486	12.7
52	1.0170	0.0151	1.46	4.951	9.7
58	0.1020	0.0235	8.23	7.154	14.0
66	4.0470	0.0235	0.75	2.631	5.1
88	4.0470	0.0574	1.89	2.997	5.9
98	2.5540	0.0898	3.94	4.273	8.3
109	2.5540	0.1400	5.87	4.642	9.1
110	4.0470	0.1400	4.46	3.455	6.7

(the sum of the radial component of drag, virtual mass, turbulent dispersion and wall force) and the ratio between bubble diameter and radial grid spacing. Compared to cases 20 and 42, case 43 has a small ratio between bubble diameter and radial grid spacing (Table 4), but the magnitude of the radial resultant force is relatively high (Fig. 11). Hence, the over-prediction in case 43 is the highest. After employing PCAM in the simulations, theses gas volume fraction peaks compared to the experimental data decrease to 250%, 20%, 70%, 10% and 30%, respectively (Fig. 10). This proves that the over-prediction of the gas volume fraction peak near the wall in the results of the Euler-Euler model can be alleviated by changing the bubble forces to act on the bubbles' centers of mass as done by PCAM.

However, not all wall peaking cases show the trend that the gas volume fraction peak simulated by using PCAM fits the peak in the experimental data better. For the wall peaking cases in Fig. 12, the gas volume fraction peaks simulated by PCAM are under-predicted. The under-prediction in cases 30, 19, 41 and 52 are about 27%, 25%, 25% and 9% of the peaks

in the experimental data, respectively. Nevertheless, the previous analysis shows that the standard Euler-Euler can have high gas concentration in the peak because of the inconsistency between the development and usage of the bubble force models. Therefore, it is possible that the agreement between the standard Euler-Euler model results and experimental data in cases 19 and 52 includes the contribution of this inconsistency. Besides, the under-prediction of the gas volume fraction peaks also exist in the results of the standard Euler-Euler simulations in cases 30 and 41. Hence, the under-prediction may results from the insufficiency in the interfacial force models or errors in the experimental data. Furthermore, the gas volume fractions in the near wall region where $0.95 < r/R < 1$ predicted by both Euler-Euler models are under-predicted. In addition, the gas volume fraction peaks in some simulation results are located further away from the wall than the locations of the peaks in the experimental data. There are two possible reasons for these results: The first reason is using the assumption of a monodisperse flow in the simulations. If bubbles smaller than the mean diameter slide on the wall or flow near the wall, the gas volume fraction peak can be located closer to the wall. The second reason is that the spatial resolution of the wire-mesh sensors in the experimental measurement is limited. As a result, they can give high gas volume fraction measurement in the measurement cell nearest to the wall if there are a lot of small bubbles flowing near the wall.

4.4. Comparison of cases with center peaks

If the gas volume fraction peaks are located in the pipe center and the bubble diameters are larger than the mesh size, an over-prediction of the gas volume fraction peaks can appear in the pipe center for standard Euler-Euler simulations. In Fig. 13, the over-prediction of the gas volume fraction peaks for standard Euler-Euler simulations is significant. Nevertheless, no improvement is found in the results of Euler-Euler model based on PCAM. Figure 14 shows that the turbulent intensity in these center peaking cases is higher than that in the wall peaking cases. A possible explaination is that the over-prediction of the gas volume fractions, which is caused by the inconsistency in the interfacial forces has been smoothed by the high turbulent dispersion. The over-prediction by both Euler-Euler models for the cases in Fig. 13 may result from using monodisperse assumption in the simulations, insufficiencies in the interfacial force models and errors in the experimental data. Besides, similar to the results in the wall peaking cases, the under-prediction of the gas volume fraction exists near the wall ($0.95 < r/R < 1$).

4.5. Comparison of cases in finely dispersed flow

In a pipe flow, a finely disperse flow regime can appear when the liquid superficial velocity is relatively high. The over-prediction of the gas volume fraction peaks in the results of the standard Euler-Euler model is significant (Fig. 15). The reason is that the magnitudes of the lift and the wall force can be as high as 10^3 N m^{-3} in the near-wall region (Fig. 16) since the liquid velocity gradient is high and the bubble diameter is small. For case 66, the gas volume fraction peak is located on the wall. This is nonphysical since the smallest distance between the peak of the gas volume fraction and the wall should be about one bubble radius in pipe flow if the bubble deformation is ignored (Lubchenko et al., 2018).

After employing PCAM, the over-prediction is alleviated (Fig. 15). Furthermore, combining PCAM with the wall-contact force avoids the gas volume fraction peak being located on the wall. Note, if the wall-contact force is a function of the gas volume fraction, it can drive too much gas away from the wall. That is the reason why it is not suggested to use it in the standard Euler-Euler model. Nevertheless, no matter which Euler-Euler model is used, the trends of the simulation results do not agree well with the trends of the experimental data even if PCAM is used. The reason can be insufficiencies in the HZDR baseline model due to some unknown effects in finely dispersed flow (Lucas et al., 2020).

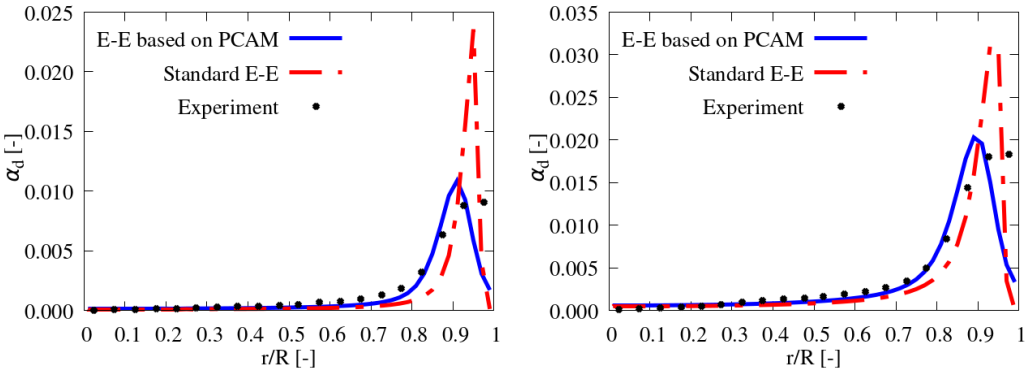

(a) Case 20.

(b) Case 42.

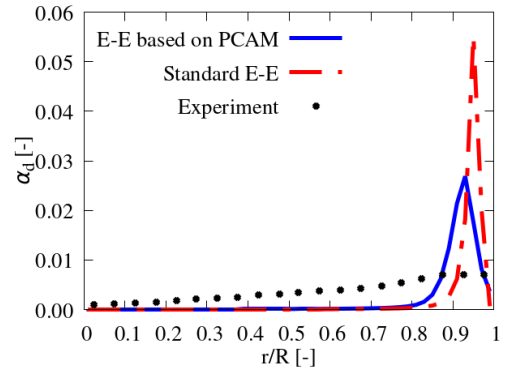

(c) Case 43.

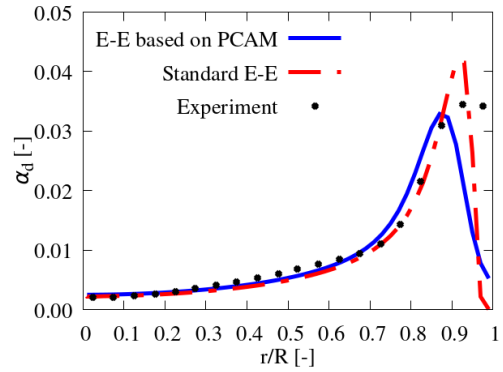

(d) Case 64.

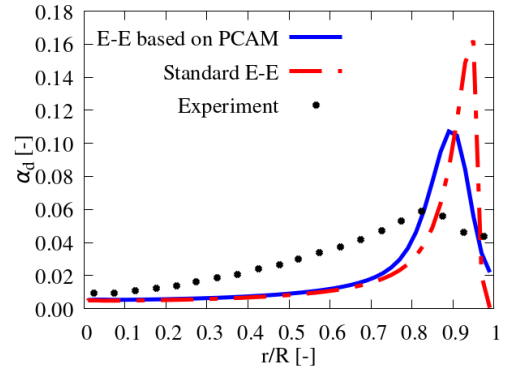

(e) Case 98.

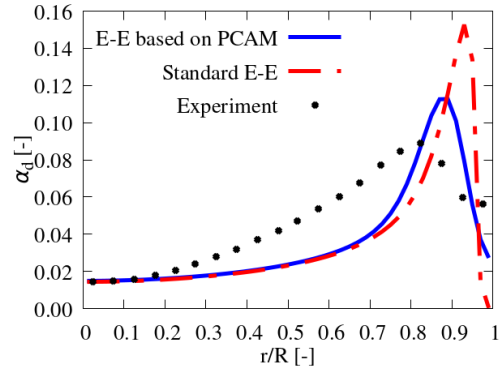

(f) Case 109.

Figure 10: Comparison of the gas volume fraction between standard Euler-Euler (E-E) and Euler-Euler based on PCAM (r: radial location; R: pipe radius).

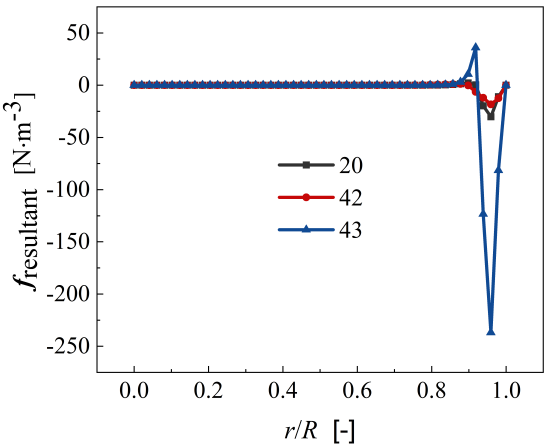

Figure 11: Radial resultant force for continuous phase in standard Euler-Euler simulations.

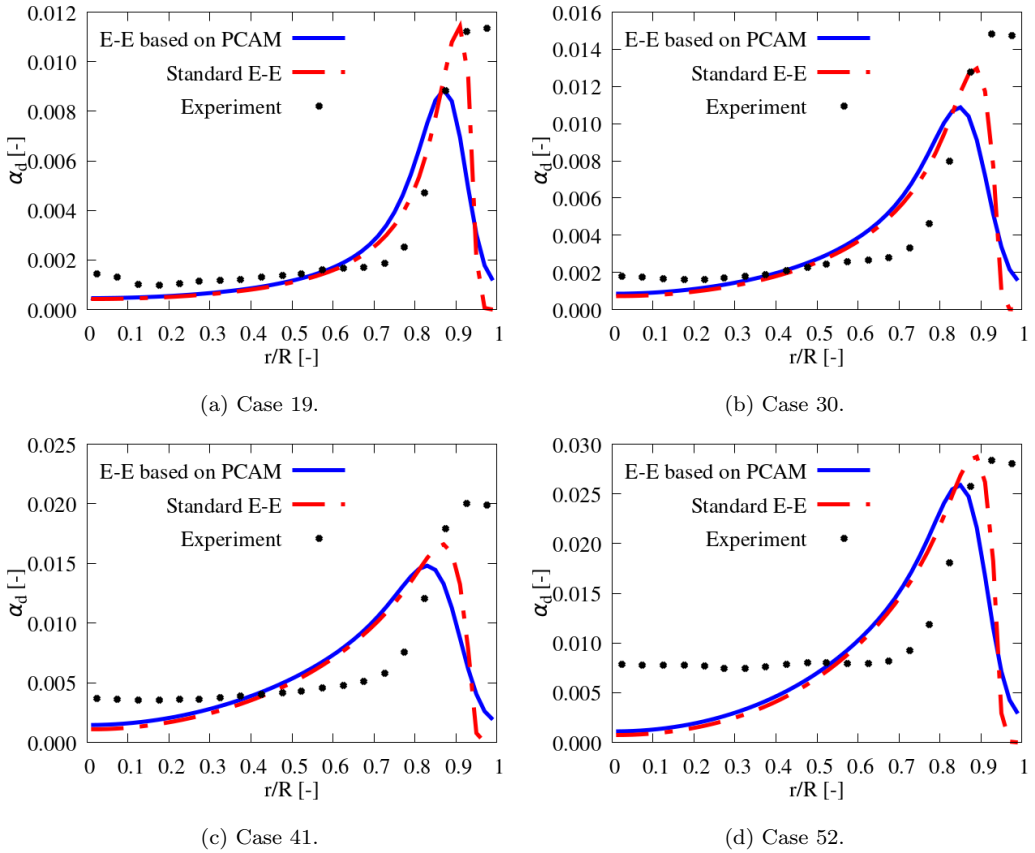

(a) Case 19.

(b) Case 30.

(c) Case 41.

(d) Case 52.

Figure 12: Gas volume fraction for wall peaking cases with under-prediction.

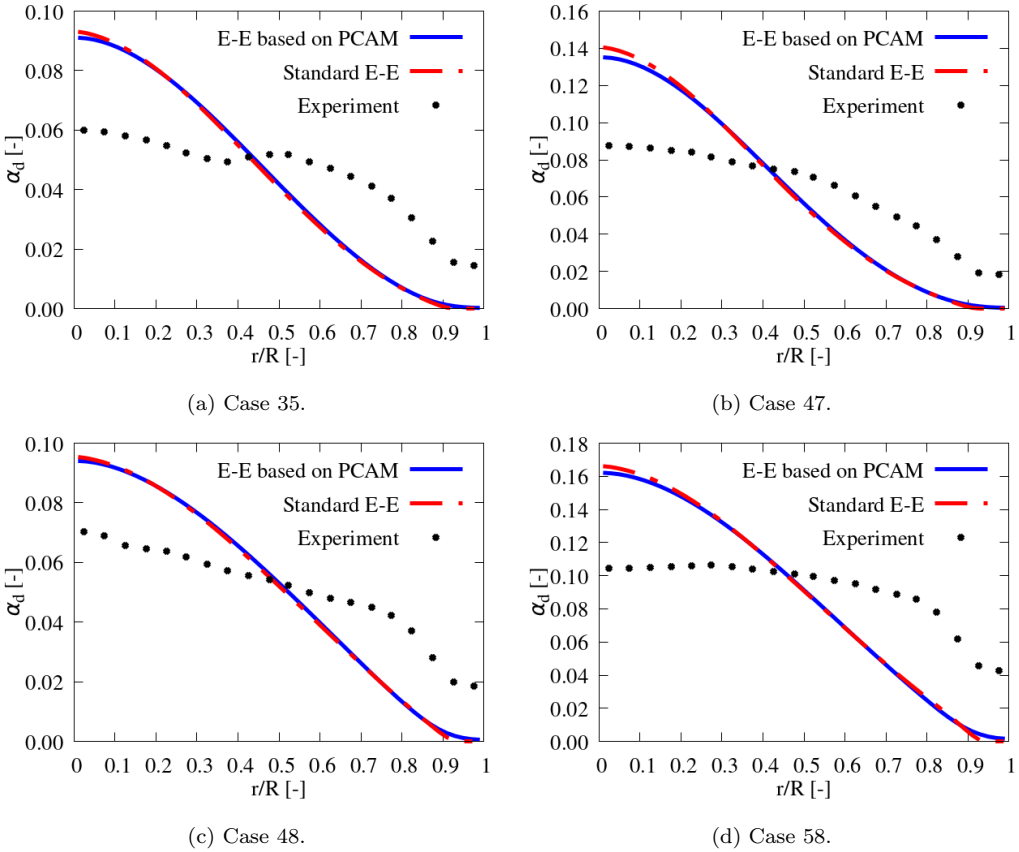

(a) Case 35.

(b) Case 47.

(c) Case 48.

(d) Case 58.

Figure 13: Gas volume fraction for center peaking cases.

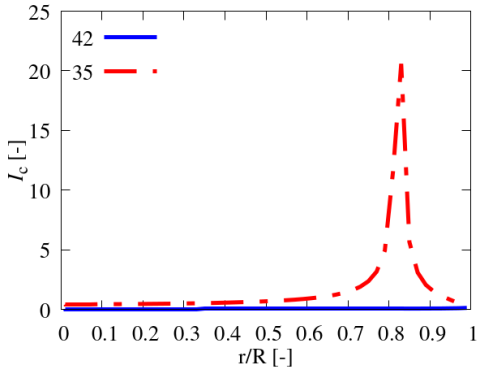

Figure 14: Turbulent intensity.

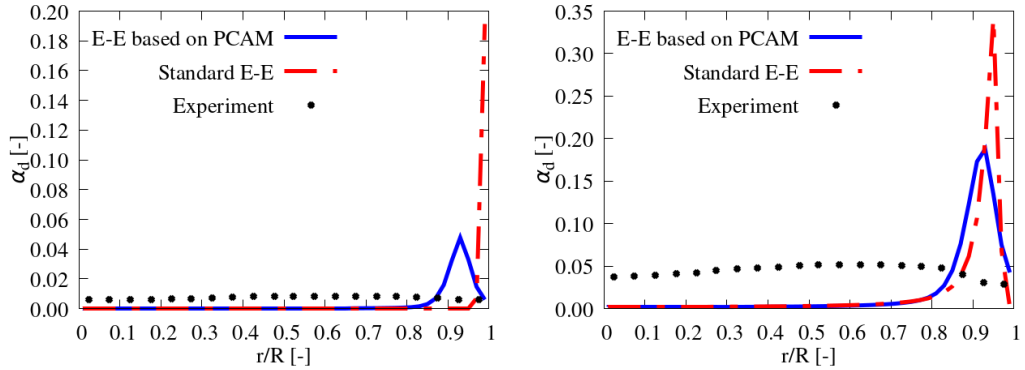

(a) Case 66. (b) Case 110.

Figure 15: Gas volume fraction for finely disperse cases.

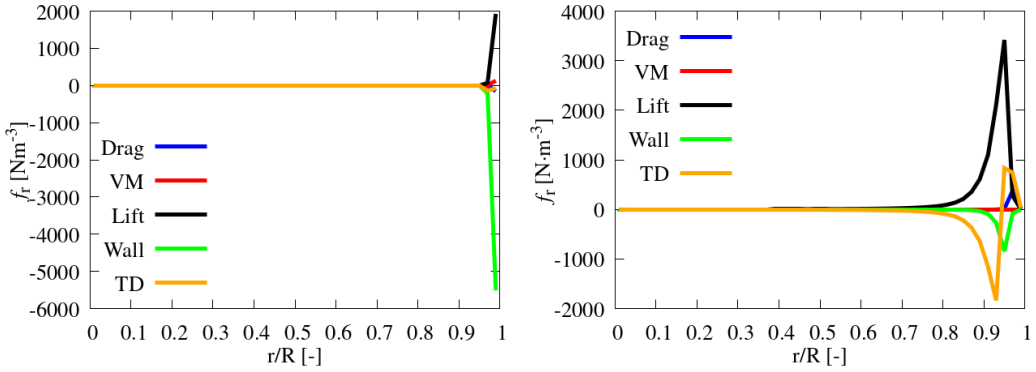

(a) Case 66. (b) Case 110.

Figure 16: Radial force component in disperse phase for finely dispersed cases (Drag: drag force; VM: virtual mass force; Lift: lift force; Wall: wall force; TD: turbulent dispersion force).

5. Summary and Conclusions

In the present study, a particle-center-averaging method is employed to recover the consistency of the interfacial forces in the Euler-Euler model. The results of a simplified two-dimensional case reveal that the inconsistency of the interfacial forces in the standard Euler-Euler model can cause the over-prediction of the gas volume fraction peaks in the channel center. Besides, a mesh independent solutions may not exist. The results show the potential of using the particle-center-averaging method to remedy these issues.

In the present bubbly pipe flows, when the ratio of bubble diameter and mesh radial spacing is between 5.1 and 14.5, the over-prediction of the gas volume fraction peak exists in a near-wall region or a pipe center for the standard Euler-Euler model. Using the particle-center-averaging method in the Euler-Euler model shows the ability to alleviate the over-prediction of the gas volume fraction peaks for some wall peaking and finely disperse cases. Moreover, it can also avoid the gas volume fraction peak being nonphysically located on the wall by introducing a wall-contact force.

Nevertheless, no improvement in the prediction of the gas volume fraction in the center peaking cases with the particle-center-averaging method is found. A possible explanation is the over-prediction of the gas volume fraction caused by the inconsistency of interfacial forces has been smoothed by the high turbulent dispersion. Besides, in majority of the simulations, some differences still exist between the measured and the simulated gas volume fractions although the particle-center-averaging method is used. The reasons may come from several aspects: First, some open questions still exist in the HZDR baseline model. Second, monodisperse simulations may not reproduce the flow phenomena in the experiments well. At last, some errors may exist in the experimental data due to the limited spatial resolution of the wire-mesh sensors and the challenges in measuring and discriminating the two phases.

In further studies, using more than one bubble velocity groups is needed. Besides, bubble coalescence and breakup are remained to be considered.

6. Acknowledgment

This work was supported by the Chinese Scholarship Council (CSC) and partly supported by the Helmholtz European Partnering Program in the project “Crossing borders and scales (Crossing)”.

7. Nomenclature

C^N	a set of all possible dynamic states	-
C_{diff}	diffusion coefficient	$\mathrm{m}^2\,\mathrm{s}^{-1}$
C_D	drag coefficient	-
C_{VM}	virtual mass coefficient	-
d	diameter	m
E	error	-
$\boldsymbol{f}$	force per unit volume	$\mathrm{N}\,\mathrm{m}^{-3}$
$\boldsymbol{g}$	acceleration of gravity	$\mathrm{m}\,\mathrm{s}^{-2}$
J	superficial velocity	$\mathrm{m}\,\mathrm{s}^{-1}$
L	distance between bubble center and wall	m
M	number of mesh cells covered by a bubble	-
n	number density of bubble centers	m^{-3}
N	the number of bubbles in the system	-
$P(N;t)$	probability density function	-
$P(\boldsymbol{x},\boldsymbol{u},t)$	one-bubble probability density function	$\mathrm{m}^{-4}\,\mathrm{s}$
p	pressure	$\mathrm{N}\,\mathrm{m}^{-2}$
r	radial coordinate	m
R	pipe radius	m
$\boldsymbol{S}$	viscous stress tensor	$\mathrm{N}\,\mathrm{m}^{-2}$
$\boldsymbol{T}$	Reynold stress tensor	$\mathrm{N}\,\mathrm{m}^{-2}$
t	time	s
$\boldsymbol{u}$	velocity vector	$\mathrm{m}\,\mathrm{s}^{-1}$
V_d	bubble volume	m^3
X_k	phase indicator function for phase k	-
x, y, z	spatial coordinates	m
$\boldsymbol{x}$, $\boldsymbol{x_0}$	spatial coordinate vector	m
x_c, $\boldsymbol{y}$	bubble center location	m
α	phase volume fraction	-
β_d	gas volume fraction projecting all bubble volume to bubble centers	-
$\delta(x)$	Dirac delta function	-
μ	dynamic viscosity	$\mathrm{kg}\,\mathrm{m}^{-1}\,\mathrm{s}^{-1}$
ρ	density	$\mathrm{kg}\,\mathrm{m}^{-3}$
τ	diffusion pseudo-time	s
σ	surface tension coefficient	$\mathrm{N}\,\mathrm{m}^{-1}$

B	bubble
c	continuous
d	disperse
k	phase index
m	mixture
exp	expected
max	maximum
opt	optimized
sol	solved
VM	virtual mass force
$\overline{\cdot}$	phase-average
$< \cdot >$	particle-center-average
$\widetilde{\cdot}$	dimensionless

Appendix

In this appendix, the derivation of turbulent dispersion force for the Euler-Euler model based on PCAM will be introduced. This derivation procedure here is similar to the procedure in Burns et al. (2004) which is used to derive the turbulent dispersion force for the standard Euler-Euler model.

Relations between time average and Favre average

For incompressible flow, the Favre average of a particle-center-averaged variable $\langle \phi_d \rangle$ is defined by

$$\widetilde{\langle \phi_d \rangle}^F = \frac{\overline{n \langle \phi_d \rangle}^t}{\overline{n}^t}, \tag{1}$$

where the tilde denotes Favre average, while the overbar and the index t represent time average. Substituting

$$\overline{n \langle \phi_d \rangle}^t = \overline{n}^t \overline{\langle \phi_d \rangle}^t + \overline{n' \langle \phi_d \rangle'}^t \tag{2}$$

into Eq. (1), we obtain

$$\overline{\langle \phi_d \rangle}^t = \widetilde{\langle \phi_d \rangle}^F - \frac{\overline{n' \langle \phi_d \rangle'}^t}{\overline{n}^t}. \tag{3}$$

A single dash ($'$) here denotes the fluctuating quantity relative to the time-averaged quantity. Replacing $\langle \phi_d \rangle$ in the last equation with $\langle \boldsymbol{u}_d \rangle$, we obtain

$$\overline{\langle \boldsymbol{u}_d \rangle}^t = \overline{\langle \boldsymbol{u}_d \rangle}^F - \frac{\overline{n' \langle \boldsymbol{u}_d \rangle'}^t}{\overline{n}^t}. \tag{4}$$

For phase-averaged velocity of the continuous phase $\overline{\boldsymbol{u}_c}$, the relation between time-averaged and Favre-averaged velocities is (Burns et al., 2004)

$$\overline{\overline{\boldsymbol{u}_c}}^t = \overline{\overline{\boldsymbol{u}_c}}^F - \frac{\overline{\alpha_c' \overline{\boldsymbol{u}_c}'}^t}{\overline{\alpha_c}^t}. \tag{5}$$

Derivation of turbulent dispersion force for the disperse phase

The drag force for the disperse phase for the Euler-Euler model based on PCAM is

$$\left\langle \boldsymbol{f}_d^{\text{drag}} \right\rangle = -D_{\text{cd, p}} A_{\text{cd}} \left(\langle \boldsymbol{u}_d \rangle - \overline{\boldsymbol{u}_c} \right), \tag{6}$$

where

$$D_{\text{cd, p}} = \frac{1}{8} C_D \rho_c \left| \langle \boldsymbol{u}_d \rangle - \overline{\boldsymbol{u}_c} \right|, \tag{7}$$

and

$$A_{\text{cd}} = n \pi d_B^2. \tag{8}$$

Note, the phase-averaged velocity of the continuous phase is used in the drag force here to keep the original definition of this quantity. It is assumed that $D_{\text{cd, p}}$ does not change with time. Applying time average to Eq.(6) yields

$$\overline{\left\langle \boldsymbol{f}_d^{\text{drag}} \right\rangle}^t = -D_{\text{cd, p}} \left[\overline{A_{\text{cd}}}^t \left(\overline{\langle \boldsymbol{u}_d \rangle}^t - \overline{\overline{\boldsymbol{u}_c}}^t \right) + \overline{A_{\text{cd}}' \left(\langle \boldsymbol{u}_d \rangle' - \overline{\boldsymbol{u}_c}' \right)}^t \right]. \tag{9}$$

Substituting Eqs. (4) and (5) into Eq. (9), we obtain

$$\begin{aligned} \overline{\left\langle \boldsymbol{f}_d^{\text{drag}} \right\rangle}^t = & - D_{\text{cd, p}} \overline{A_{\text{cd}}}^t \left[\left(\overline{\langle \boldsymbol{u}_d \rangle}^F - \frac{\overline{n' \langle \boldsymbol{u}_d \rangle'}^t}{\overline{n}^t} \right) - \left(\overline{\overline{\boldsymbol{u}_c}}^F - \frac{\overline{\alpha_c' \overline{\boldsymbol{u}_c}'}^t}{\overline{\alpha_c}^t} \right) \right] \\ & - D_{\text{cd, p}} \overline{A_{\text{cd}}' \left(\langle \boldsymbol{u}_d \rangle' - \overline{\boldsymbol{u}_c}' \right)}^t \end{aligned} \tag{10}$$

The last equation can be simplified to

$$\overline{\left\langle \boldsymbol{f}_d^{\text{drag}} \right\rangle}^t = -D_{\text{cd, p}} \overline{A_{\text{cd}}}^t \left(\overline{\langle \boldsymbol{u}_d \rangle}^F - \overline{\overline{\boldsymbol{u}_c}}^F \right) + \boldsymbol{f}_d^{\text{TD}}, \tag{11}$$

where

$$\boldsymbol{f}_d^{\mathrm{TD}} = D_{\mathrm{cd,\,p}}\overline{A_{\mathrm{cd}}}^t\left(\frac{\overline{n'\langle\boldsymbol{u}_d\rangle'}^t}{\overline{n}^t} - \frac{\overline{\alpha_c{}'\overline{\boldsymbol{u}_c}'}^t}{\overline{\alpha_c}^t}\right) - D_{\mathrm{cd,\,p}}\overline{A_{\mathrm{cd}}{}'\left(\langle\boldsymbol{u}_d\rangle' - \overline{\boldsymbol{u}_c}'\right)}^t. \tag{12}$$

Substituting

$$\overline{C_{\mathrm{cd,\,p}}}^t = D_{\mathrm{cd,\,p}}\overline{A_{\mathrm{cd}}}^t \tag{13}$$

into Eq. (12) results in

$$\boldsymbol{f}_d^{\mathrm{TD}} = \overline{C_{\mathrm{cd,\,p}}}^t\left(\frac{\overline{n'\langle\boldsymbol{u}_d\rangle'}^t}{\overline{n}^t} - \frac{\overline{\alpha_c{}'\overline{\boldsymbol{u}_c}'}^t}{\overline{\alpha_c}^t}\right) - \overline{C_{\mathrm{cd,\,p}}}^t\frac{\overline{A_{\mathrm{cd}}{}'\left(\langle\boldsymbol{u}_d\rangle' - \overline{\boldsymbol{u}_c}'\right)}^t}{\overline{A_{\mathrm{cd}}}^t}. \tag{14}$$

Bubble diameter is a constant. Therefore

$$A_{\mathrm{cd}}{}' = n'\pi d_B^2, \tag{15}$$

and

$$\overline{A_{\mathrm{cd}}}^t = \overline{n}^t\pi d_B^2. \tag{16}$$

Based on Eqs. (15) and (16), we have

$$\frac{\overline{A_{\mathrm{cd}}{}'\left(\langle\boldsymbol{u}_d\rangle' - \overline{\boldsymbol{u}_c}'\right)}^t}{\overline{A_{\mathrm{cd}}}^t} = \frac{\overline{n'\left(\langle\boldsymbol{u}_d\rangle' - \overline{\boldsymbol{u}_c}'\right)}^t}{\overline{n}^t}. \tag{17}$$

Substituting Eq. (17) into Eq. (14) and simplifying it, we obtain

$$\boldsymbol{f}_d^{\mathrm{TD}} = \overline{C_{\mathrm{cd,\,p}}}^t\left(\frac{\overline{n'\overline{\boldsymbol{u}_c}'}^t}{\overline{n}^t} - \frac{\overline{\alpha_c'\overline{\boldsymbol{u}_c}'}^t}{\overline{\alpha_c}^t}\right). \tag{18}$$

Using the eddy diffusivity hypothesis in the modeling of the turbulence related terms, we have

$$\overline{n'\overline{\boldsymbol{u}_c}'}^t = -\frac{\upsilon_c^{\mathrm{turb}}}{\sigma_{\mathrm{nc}}}\nabla\overline{n}^t, \tag{19}$$

and

$$\overline{\alpha_c'\overline{\boldsymbol{u}_c}'}^t = -\frac{\upsilon_c^{\mathrm{turb}}}{\sigma_{\alpha\mathrm{c}}}\nabla\overline{\alpha_c}^t, \tag{20}$$

After substituting Eqs. (19) and (20) into Eq. (18), we have

$$\boldsymbol{f}_d^{\mathrm{TD}} = -\overline{C_{\mathrm{cd,\,p}}}^t\left(\frac{\upsilon_c^{\mathrm{turb}}}{\sigma_{\mathrm{nc}}}\frac{\nabla\overline{n}^t}{\overline{n}^t} - \frac{\upsilon_c^{\mathrm{turb}}}{\sigma_{\alpha\mathrm{c}}}\frac{\nabla\overline{\alpha_c}^t}{\overline{\alpha_c}^t}\right). \tag{21}$$

Here, we assumed that

$$\sigma_{\mathrm{nc}} = \sigma_{\alpha\mathrm{c}}. \tag{22}$$

Since $\beta_d = nV_d$ and the bubble volume V_d is a constant, we have

$$\frac{\nabla \overline{n}^t}{\overline{n}^t} = \frac{\nabla \overline{\beta_d}^t}{\overline{\beta_d}^t}. \tag{23}$$

Substituting Eqs. (22) and (23) into Eq. (21), we obtain

$$\boldsymbol{f}_d^{\mathrm{TD}} = -\overline{C_{\mathrm{cd,\,p}}}^t \frac{\upsilon_c^{\mathrm{turb}}}{\sigma_{\alpha\mathrm{c}}} \left(\frac{\nabla \overline{\beta_d}^t}{\overline{\beta_d}^t} - \frac{\nabla \overline{\alpha_c}^t}{\overline{\alpha_c}^t} \right). \tag{24}$$

497 Comparing the last equation with the turbulent dispersion force model in
498 Burns et al. (2004), we can find that $\nabla\alpha_d/\alpha_d$ is changed to $\nabla\beta_d/\beta_d$ here.

References

Biesheuvel, A., Gorissen, W., 1990. Void fraction disturbances in a uniform bubbly fluid. International Journal of Multiphase Flow 16, 211–231.

Bokkers, G., Laverman, J., van Sint Annaland, M., Kuipers, J., 2006. Modelling of large-scale dense gas–solid bubbling fluidised beds using a novel discrete bubble model. Chemical Engineering Science 61, 5590–5602.

Burns, A.D., Frank, T., Hamill, I., Shi, J.M., et al., 2004. The Favre averaged drag model for turbulent dispersion in Eulerian multi-phase flows, in: 5th International Conference on Multiphase Flow, International Conference on Multiphase Flow. pp. 1–17.

Darmana, D., Deen, N.G., Kuipers, J., 2006. Parallelization of an Euler–Lagrange model using mixed domain decomposition and a mirror domain technique: Application to dispersed gas–liquid two-phase flow. Journal of Computational Physics 220, 216–248.

Deen, N.G., van Sint Annaland, M., Kuipers, J., 2004. Multi-scale modeling of dispersed gas–liquid two-phase flow. Chemical Engineering Science 59, 1853–1861.

Drew, D.A., Passman, S.L., 1998. Theory Multicomponent Fluids. volume 135. Springer-Verlag.

Fleck, S., Rzehak, R., 2019. Investigation of bubble plume oscillations by euler-euler simulation. Chemical Engineering Science 207, 853–861.

Haberman, R., 2012. Applied partial differential equations with Fourier series and boundary value problems. Pearson Higher Ed.

Hänsch, S., Evdokimov, I., Schlegel, F., Lucas, D., 2021. A workflow for the sustainable development of closure models for bubbly flows. Chemical Engineering Science , 116807.

Hosokawa, S., Tomiyama, A., Misaki, S., Hamada, T., 2002. Lateral migration of single bubbles due to the presence of wall, in: Fluids Engineering Division Summer Meeting, pp. 855–860.

Ishii, M., Zuber, N., 1979. Drag coefficient and relative velocity in bubbly, droplet or particulate flows. AIChE journal 25, 843–855.

Krepper, E., Rzehak, R., Lucas, D., 2018. Validation of a closure model framework for turbulent bubbly two-phase flow in different flow situations. Nuclear Engineering and Design 340, 388–404.

Lau, Y., Bai, W., Deen, N., Kuipers, J., 2014. Numerical study of bubble break-up in bubbly flows using a deterministic Euler–Lagrange framework. Chemical Engineering Science 108, 9–22.

Lau, Y., Roghair, I., Deen, N., van Sint Annaland, M., Kuipers, J., 2011. Numerical investigation of the drag closure for bubbles in bubble swarms. Chemical Engineering Science 66, 3309–3316.

Lehnigk, R., 2021. A generalized population balance model for the simulation of polydisperse multiphase flows within the Euler-Euler framework. Ph.D. thesis. Technische Universität Dresden. Dresden, Germany.

Liao, J., Ziegenhein, T., Rzehak, R., 2016. Bubbly flow in an airlift column: a cfd study. Journal of Chemical Technology & Biotechnology 91, 2904–2915.

Liao, Y., Ma, T., Krepper, E., Lucas, D., Fröhlich, J., 2019. Application of a novel model for bubble-induced turbulence to bubbly flows in containers and vertical pipes. Chemical Engineering Science 202, 55–69.

Liao, Y., Ma, T., Liu, L., Ziegenhein, T., Krepper, E., Lucas, D., 2018. Eulerian modelling of turbulent bubbly flow based on a baseline closure concept. Nuclear Engineering and Design 337, 450–459.

Liao, Y., Upadhyay, K., Schlegel, F., 2020. Eulerian-Eulerian two-fluid model for laminar bubbly pipe flows: Validation of the baseline model. Computers & Fluids 202, 104496.

Lubchenko, N., Magolan, B., Sugrue, R., Baglietto, E., 2018. A more fundamental wall lubrication force from turbulent dispersion regularization for multiphase cfd applications. International Journal of Multiphase Flow 98, 36–44.

Lucas, D., Krepper, E., Liao, Y., Rzehak, R., Ziegenhein, T., 2020. General guideline for closure model development for gas-liquid flows in the multi-fluid framework. Nuclear Engineering and Design 357, 110396.

Lucas, D., Krepper, E., Prasser, H.M., 2001. Prediction of radial gas profiles in vertical pipe flow on the basis of bubble size distribution. International Journal of Thermal Sciences 40, 217–225.

Lucas, D., Krepper, E., Prasser, H.M., 2005. Development of co-current air–water flow in a vertical pipe. International Journal of Multiphase Flow 31, 1304–1328.

Lucas, D., Krepper, E., Prasser, H.M., 2007. Use of models for lift, wall and turbulent dispersion forces acting on bubbles for poly-disperse flows. Chemical Engineering Science 62, 4146–4157.

Lyu, H., Schlegel, F., Rzehak, R., Lucas, D., 2020. Improvement of euler-euler simulation of two-phase flow by particle-center-averaged method, in: 14th International Conference on CFD in 6 Oil & Gas, Metallurgical and Process Industries SINTEF, Trondheim, Norway, October 12–14, 2020, SINTEF Academic Press.

Ma, T., Santarelli, C., Ziegenhein, T., Lucas, D., Fröhlich, J., 2017. Direct numerical simulation–based reynolds-averaged closure for bubble-induced turbulence. Physical Review Fluids 2, 034301.

Moraga, F., Larreteguy, A., Drew, D., Lahey Jr, R., 2006. A center-averaged two-fluid model for wall-bounded bubbly flows. Computers & Fluids 35, 429–461.

OpenFOAM Foundation, 2020. OpenFOAM-dev. URL: https://github.com/OpenFOAM/OpenFOAM-dev/tree/7dd592ff4013fc6e444f27b12ff8729774cb5e0f/applications/solvers/multiphase/reactingEulerFoam/reactingTwoPhaseEulerFoam.

Prosperetti, A., 1998. Ensemble averaging techniques for disperse flows, in: Particulate Flows. Springer, pp. 99–136.

Prosperetti, A., Jones, A., 1984. Pressure forces in disperse two-phase flow. International Journal of Multiphase Flow 10, 425–440.

Rzehak, R., Krauß, M., Kováts, P., Zähringer, K., 2017a. Fluid dynamics in a bubble column: New experiments and simulations. International Journal of Multiphase Flow 89, 299–312.

Rzehak, R., Krepper, E., 2015. Bubbly flows with fixed polydispersity: validation of a baseline closure model. Nuclear Engineering and Design 287, 108–118.

Rzehak, R., Ziegenhein, T., Kriebitzsch, S., Krepper, E., Lucas, D., 2017b. Unified modeling of bubbly flows in pipes, bubble columns, and airlift columns. Chemical Engineering Science 157, 147–158.

Shi, P., Rzehak, R., 2018. Bubbly flow in stirred tanks: Euler-Euler/RANS modeling. Chemical Engineering Science 190, 419–435.

Sun, R., Xiao, H., 2015a. Diffusion-based coarse graining in hybrid continuum–discrete solvers: Applications in CFD–DEM. International Journal of Multiphase Flow 72, 233–247.

Sun, R., Xiao, H., 2015b. Diffusion-based coarse graining in hybrid continuum–discrete solvers: theoretical formulation and a priori tests. International Journal of Multiphase Flow 77, 142–157.

Tomiyama, A., Shimada, N., Asano, H., 2003. Application of number density transport equation for the recovery of consistency in multi-field model, in: Fluids Engineering Division Summer Meeting, pp. 501–508.

Tomiyama, A., Tamai, H., Zun, I., Hosokawa, S., 2002. Transverse migration of single bubbles in simple shear flows. Chemical Engineering Science 57, 1849–1858.

Zhang, D., Prosperetti, A., 1994. Averaged equations for inviscid disperse two-phase flow. Journal of Fluid Mechanics 267, 185–219.

Zhang, D., Prosperetti, A., 1995. Energy and momentum equations for disperse two-phase flows and their closure for dilute suspensions. Journal of Fluid Mechanics .

Zhang, D., Prosperetti, A., 1997. Momentum and energy equations for disperse two-phase flows and their closure for dilute suspensions. International Journal of Multiphase Flow 23, 425–453.

Zidouni, F., Krepper, E., Rzehak, R., Rabha, S., Schubert, M., Hampel, U., 2015. Simulation of gas–liquid flow in a helical static mixer. Chemical Engineering Science 137, 476–486.

Ziegenhein, T., Rzehak, R., Krepper, E., Lucas, D., 2013. Numerical simulation of polydispersed flow in bubble columns with the inhomogeneous multi-size-group model. Chemie Ingenieur Technik 85, 1080–1091.

Ziegenhein, T., Tomiyama, A., Lucas, D., 2018. A new measuring concept to determine the lift force for distorted bubbles in low morton number system: Results for air/water. International Journal of Multiphase Flow 108, 11–24.